OBSERVATIONAL CONSTRAINTS ON BLUE PRIMORDIAL SPECTRA

FRANCESCO LUCCHIN,[1] SERGIO COLAFRANCESCO,[2] GIANCARLO DE GASPERIS,[3] SABINO MATARRESE,[4]
SIMONA MEI,[5] SILVIA MOLLERACH,[6] LAURO MOSCARDINI,[1] AND NICOLA VITTORIO[7]

ABSTRACT

Recently, there has been growing interest in primordial "blue" ($n > 1$) perturbation spectra, motivated both by a composite set of observational data on large scales and from the point of view of theoretical model building. After reviewing the theoretical (inflationary) motivations for these blue spectra, we consider various observational constraints, within both cold dark matter and mixed dark matter scenarios. In particular, using linear theory, we discuss large-scale bulk flows and the X-ray cluster abundance. We also perform various N-body simulations of these models to study the clustering properties of the matter distribution and the peculiar velocity field.

Subject headings: cosmology: theory — dark matter — galaxies: clusters: general — methods: numerical

1. INTRODUCTION

The anisotropy of the cosmic microwave background (CMB), detected on large angular scales by *COBE* (Smoot et al. 1992; Bennett et al. 1994), provides insight into primordial perturbations. This measurement yields, on the one hand, the amplitude of density perturbations at the largest observable scales, and, on the other hand, the spectral index n, which fully determines the power spectrum [i.e., $P(k) \propto Ak^n$] of the primordial density fluctuation field, up to a possible contribution by a stochastic background of gravitational waves. These constraints, promptly taken into account in the current cosmological debate, can discriminate among the possible scenarios. In particular, the standard (i.e., $n = 1$) cold dark matter (SCDM) model with the *COBE* normalization predicts too much structure on scales $\lesssim 10\ h^{-1}$ Mpc (where h is the Hubble constant in units of 100 km s^{-1} Mpc^{-1}), e.g., in terms of an excessive abundance of clusters (e.g., White, Efstathiou, & Frenk 1993; Colafrancesco & Vittorio 1994), and of too large rms pairwise galaxy velocities on megaparsec scales (Davis et al. 1985; see, however, Mo, Jing, & Borner 1993; Zurek et al. 1994). Tilted (i.e., $n < 1$) CDM models are in better agreement with observations on small scales, but the amount of tilting is strongly constrained by data on the large-scale velocity field (Moscardini et al. 1995) and by cluster clustering properties (Plionis et al. 1995). The most severe flaw of tilted CDM models is the very late epoch of galaxy formation.

A fashionable alternative to SCDM, which has recently emerged to overcome these problems, is provided by mixed (i.e., cold + hot) dark matter (MDM) models: adding to the cold dark matter a small contribution ($\sim 10\%$–30% of the critical density) of massive neutrinos erases, via free streaming, part of the power on the scales of galaxies and clusters. This scenario will also be reinforced from the particle physics side, if recent claims for a mass of order 2 eV for the μ neutrino are confirmed (Louis 1994). The standard MDM model is based on the same assumptions as SCDM; in particular, the primordial power spectrum is assumed again to be scale-invariant (i.e., $n = 1$). Although the results of linear analyses and numerical simulations (e.g., Klypin et al. 1993; see also Davis, Summers, & Schlegel 1992; Schaefer & Shafi 1993; Jing et al. 1994; Cen & Ostriker 1994; Klypin, Nolthenius, & Primack 1995b) are certainly promising, some problems are clearly present: an example is the excessive delay of the epoch of galaxy formation, in contrast to observations of quasars and damped Lyα systems at redshifts $z \geq 3$ (Ma & Bertschinger 1994; Klypin et al. 1995a).

The analysis of the first 2 years of the *COBE* DMR data indicates a most likely value for the spectral index in the range $n = 0.9$–1.9 (Bennett et al. 1994; see also Górski et al. 1994), a value also suggested by the Tenerife experiment at 5° (Hancock et al. 1994) and by the MAX measurements at 1° (e.g., Gundersen et al. 1993; Devlin et al. 1994). An $n > 1$ perturbation spectrum can also be at the origin of the claimed bulk flow on scales of 150 h^{-1} Mpc (Lauer & Postman 1994) and of the large voids in the galaxy distribution of the CfA survey (de Lapparent, Geller, & Huchra 1986; Geller & Huchra 1989), at scales of order 50 h^{-1} Mpc, as pointed out by Piran et al. (1993). On the other hand, it is also possible to put upper bounds on the value of n. Carr & Lidsey (1993) found $n < 1.5$, from primordial black hole overproduction constraints on nucleosynthesis and the *COBE* data (see also Carr, Gilbert, & Lidsey 1994). Hu, Scott, & Silk (1994) set an independent constraint, $n < 1.54$, by using recent experimental limits on the CMB spectral distortions found by *COBE* FIRAS.

Most theories for the origin of the primordial fluctuations predict a spectral index $n \leq 1$. In particular, inflationary models based on simple inflation potentials originate this type of spectra. Nevertheless, in recent years some authors have pointed out that suitable inflationary dynamics can easily account for blue spectra (Liddle & Lyth 1993; Linde 1994; Mollerach, Matarrese, & Lucchin 1994; Copeland et

[1] Dipartimento di Astronomia, Università di Padova, vicolo dell'Osservatorio 5, I-35122 Padova, Italy.

[2] Osservatorio Astronomico di Roma, via dell'Osservatorio 5, I-00040 Monteporzio (RM), Italy.

[3] Dipartimento di Fisica, Università dell'Aquila, via Vetoio 1, I-67010 Coppito (AQ), Italy.

[4] Dipartimento di Fisica G. Galilei, Università di Padova, via Marzolo 8, I-35131 Padova, Italy.

[5] Université Louis Pasteur, Observatorie Astronomique de Strasbourg, 11 rue de l'Université, F-67000 Strasbourg, France.

[6] Scuola Internazionale Superiore di Studi Avanzati, via Beirut 2–4, I-34013 Trieste, Italy.

[7] Dipartimento di Fisica, Università di Roma "Tor Vergata," via della Ricerca Scientifica, I-00133 Roma, Italy.

al. 1994), in particular, in the framework of the so-called hybrid models.

In this paper we investigate the predictions of a possible variant of MDM models, by assuming a "blue," i.e., $n > 1$, primordial density perturbation spectrum; this blue mixed dark matter (BMDM) model, suitably normalized to *COBE* DMR, may alleviate the small-scale problem of the standard (i.e., $n = 1$) MDM model. An important advantage of "antitilting" the spectrum is that it provides an earlier galaxy formation epoch (see, e.g., Borgani et al. 1995). Here we restrict ourselves to discussion of the present matter and light distribution, in both the linear and the nonlinear regime. We refer to de Bernardis, Balbi, & Vittorio (1995) for a discussion of how MDM models compare with the anisotropy data at degree angular scales.

The plan of the paper is as follows. In § 2 we discuss the theoretical motivation for blue power spectra from the inflationary point of view. In § 3 we show the predictions of the linear theory for the large-scale peculiar velocities and for the galaxy cluster abundance. In § 4 we present the analysis of our *N*-body simulations. Finally, in § 5 we discuss our results and draw our main conclusions.

2. INFLATIONARY MODELS

Quantum fluctuations of scalar fields during inflation provide a very appealing explanation for the origin of the primordial density perturbations. It is useful to describe these perturbations in terms of the gauge-invariant variable ζ. Its power spectrum to first order in the slow-roll approximation is given by

$$P_\zeta^{1/2}(k) = \left.\frac{H^2}{2\pi\dot\phi}\right|_{aH=k} . \quad (1)$$

Its spectral index, defined by $\alpha \equiv d \ln P_\zeta^{1/2}/d \ln k$, is related to the spectral index of density perturbations on constant-time hypersurfaces before matter-radiation equality as $n = 2\alpha + 1$. Most inflationary models predict a spectral index $n < 1$. This is the case, for example, for models based on a polynomial potential, which give rise to a power-spectrum $P_\zeta^{1/2}(k)$ logarithmically decreasing with k. Another example is the power-law inflation, which is based on an exponential potential and gives rise to a power-spectrum decreasing with k as a power (Lucchin & Matarrese 1985). This is due to the fact that in most inflationary models $H^2/|\dot\phi|$ decreases with time as the inflaton evolves, thus the larger wavenumber perturbations, which left the horizon later, have smaller amplitude. However, as discussed recently by Mollerach et al. (1994), there is a class of simple inflationary models leading to density perturbations with $n > 1$ (see also Liddle & Lyth 1993; Carr & Lidsey 1993; Linde 1994; Copeland et al. 1994). These are produced while the inflaton field rolls down to a potential minimum with potential energy dominated by a cosmological constant–like piece. In this case $|\dot\phi|$ decreases as ϕ approaches the potential minimum, while H^2 remains approximately constant in such a way that $H^2/|\dot\phi|$ increases with time. The shape of the inflaton potential leading to $P_\zeta^{1/2}(k) \propto k^\alpha$ with $\alpha = \text{constant} > 0$ has been obtained by Mollerach et al. (1994); it looks quite complicated. However, if the condition that α is constant for all scales is relaxed, a huge class of potentials with a nonvanishing energy density in the minimum, which corresponds to an effective cosmological

constant, can work. For example, the potentials $V(\phi) = V_0 + f\phi^m$ give rise to a spectrum decreasing with k for wavelengths that left the Hubble radius when $f\phi^m > V_0$,

$$n \simeq 1 + \frac{2fm(m-1)}{\kappa^2 V_0}\phi^{m-2} , \quad (2)$$

where the right-hand side has to be evaluated at the time when the wavelengths of interest left the horizon during inflation. In particular, we see that the quadratic potential case, $m = 2$, gives rise to an approximately constant spectral index $n > 1$.

One can think that these kinds of potentials will have problems in ending inflation and reheating the universe, as the two usual reheating mechanisms, namely, rapid oscillations of the inflaton field around the potential minimum and first-order phase transitions with bubble production, do not work in this case. This reheating problem can nevertheless be avoided by the "hybrid inflation" mechanism, recently proposed by Linde (1991a, b, 1994). According to it, inflation ends in the following way: the slow roll of the inflaton field at a given time triggers a second-order phase transition of a second field, whose false vacuum energy density is responsible for the cosmological constant term. The field rolls down to its potential minimum and oscillates around it. A particular potential in which this scenario can be realized is (Linde 1991a, b, 1994)

$$V(\phi, \sigma) = \frac{1}{4\lambda}(M^2 - \lambda\sigma^2)^2 + \frac{m^2}{2}\phi^2 + \frac{g^2}{2}\phi^2\sigma^2 . \quad (3)$$

For $\phi > \phi_c \equiv M/g$, σ is in its false vacuum at $\sigma = 0$. The potential for ϕ in this regime is given by $V(\phi) = M^4/4\lambda + m^2\phi^2/2$. As we have discussed, when the cosmological constant term dominates, this gives rise to an inflationary phase with a power spectrum $P_\zeta(k)$ increasing with k. From equation (2), the spectral index for the perturbations is given by $\alpha \simeq 4\lambda m^2/\kappa^2 M^4$. To be consistent with the approximations done, this result holds only for small values of α. For a given value of α, this fixes the relation between m^2 and M^4. When $\phi < \phi_c$, σ rolls down to its minimum and the universe reheats.

There are some constraints on the model parameters in order for it to work. In order to have at least 60 *e*-foldings of inflation for $\phi > \phi_c$, one needs $M^3 \gtrsim m^2\lambda e^{60\alpha}M_P/g$, and in order for inflation to finish soon after ϕ reaches ϕ_c, one needs $M^6 \lesssim 3\lambda^2 M_P^4 m^2/2\pi^2$. Here M_P is the Planck mass.

The amplitude of the perturbations that left the horizon around 60 *e*-foldings before the end of inflation (the ones relevant for structure formation) is given by

$$P_\zeta^{1/2}(k_{60}) = \frac{(2\pi)^{1/2}gM^5}{\sqrt{3}\,\lambda^{3/2}M_P^3 m^2}\exp\left(-60\,\frac{4\lambda m^2}{\kappa^2 M^4}\right) . \quad (4)$$

If we normalize its amplitude using the *COBE* $Q_{rms\text{-}PS}$ determination, we obtain

$$P_\zeta(k_{60}) \equiv A^2(n) = (Q_{rms\text{-}PS}/T_0)^2 40\Gamma^2(2 - n/2)$$
$$\times\ \Gamma(\tfrac{9}{2} - n/2)/\pi\Gamma(3 - n)\Gamma(\tfrac{3}{2} + n/2) .$$

From the analysis of the first 2 years of *COBE* data, $Q_{rms\text{-}PS} = 18.2e^{0.58(1-n)}\ \mu K$ (Bennett et al. 1994) and the FIRAS value $T_0 = 2.726 \pm 0.010$ K (Mather et al. 1994), the resulting values of $A(n)$ are of the order of 4×10^{-5} for the values of n of interest. This normalization, combined with

the previous relation between m^2 and M^4 in terms of α, gives the values of m and M:

$$M \simeq 4.3A(n)\alpha e^{60\alpha} \frac{\lambda^{1/2}}{g} M_P \,,$$

$$m \simeq 47A^2(n)\alpha^{5/2}e^{120\alpha} \frac{\lambda^{1/2}}{g^2} M_P \,. \tag{5}$$

For a given value of α these relations fix the values of m and M. We have to verify that the constraints imposed on the model parameters are satisfied. The condition $M^2\phi^2/2 < M^4/4\lambda$ translates to $\lambda^{1/4} < 50e^{-60\alpha}g/\alpha^{3/4}$. We can ensure that this is satisfied for all the values of α of interest taking for the coupling constants $g \sim O(1)$ and λ small enough. The condition for inflation to end soon after $\phi \sim \phi_c$ holds only for $\alpha \lesssim 0.17$ ($n \lesssim 1.35$). The additional constraint that the energy density be smaller that the Planck density, $M^4/4\lambda < M_P^4$, always holds when the above conditions are satisfied.

3. LINEAR TESTS OF BLUE PRIMORDIAL SPECTRA

Following the inflationary paradigm, we restrict ourselves to flat cosmological models, where a Hubble parameter $h = 0.5$ is assumed and baryons contribute only for the 5% to the critical density (i.e., $\Omega_B = 0.05$). The fractions of the critical density in cold and hot dark matter are $\Omega_{CDM} = 1 - \Omega_B - \Omega_v$, and $\Omega_{HDM} = \Omega_v$, respectively. The family of flat MDM model is then characterized only by the parameter Ω_v, which in this section we allow to vary between 0 (pure CDM) and $\lesssim 0.5$ (the MDM model where hierarchical clustering still occurs).

In order to study the present matter distribution in MDM models, we evaluate the transfer function of density fluctuations in each of the four components (CDM, HDM, baryons, photons) by numerically integrating the full set of equations for the perturbed matter–energy density field in the synchronous gauge formalism. The details of our calculation are described in de Gasperis, Muciaccia, & Vittorio (1995; see also Peebles 1981; Bonometto et al. 1984). The results for $\Omega_v = 0.3$ are shown in Figure 1, where we plot the transfer function $T(k)$ for each separate component: CDM, HDM, and baryons, respectively. Here we assume that there is only one family of massive neutrinos. So $\Omega_v = 0.3$ corresponds to a neutrino mass $m_v \approx 7$ eV. We also plot the total transfer function defined as follows:

$$T_{TOT}(k) = \Omega_{CDM} T_{CDM}(k) + \Omega_v T_v(k) + \Omega_B T_B(k) \,. \tag{6}$$

The transfer function is given in arbitrary units. However, the relative amplitude of $T(k)$ at different redshifts reflects the linear growth of density fluctuation in an Einstein–de Sitter universe. We evaluated the transfer functions at redshift $z = 20$, in order to start our N-body calculations properly (see next section), with the right statistical segregation among the different components. In Figure 1 it is evident that baryons (*dotted line*) catch up completely with the CDM (*dashed line*) at the present time. The transfer function of massive neutrinos (*long-dashed line*) is initially lower than the CDM one because of free streaming. However, it becomes presently comparable to that of the other components, at least for the range of wavenumbers shown in Figure 1.

Figure 2 shows the rms value of the density fluctuation field at the present time, $\sigma(R)$, smoothed with a top-hat filter
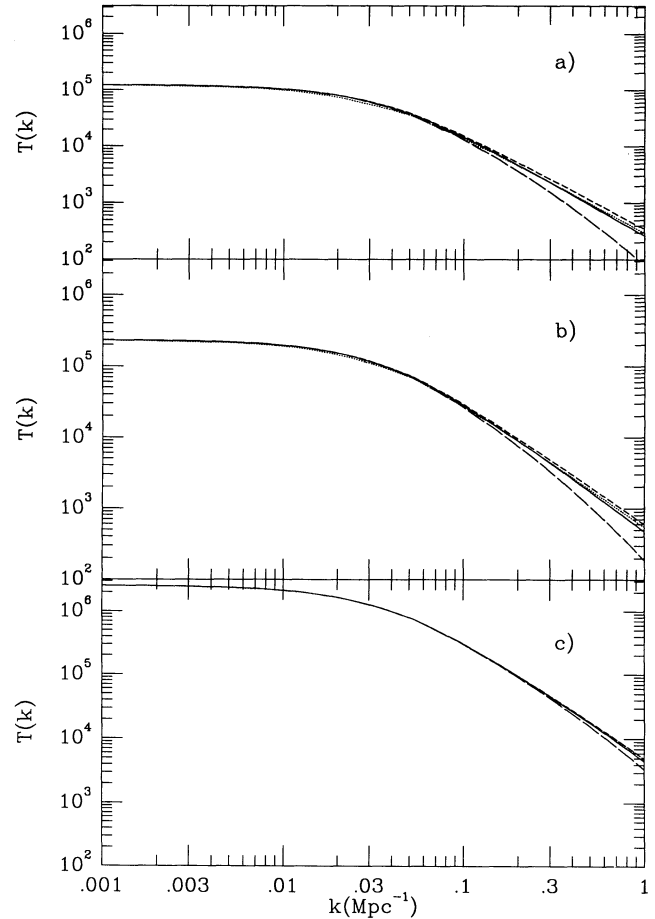

FIG. 1.—Total transfer function (*solid line*) and transfer function for baryonic (*dotted line*), cold (*dashed line*) and hot (*long-dashed line*) components, at different redshifts: (*a*) $z = 20$; (*b*) $z = 10$; (*c*) the present time, $z = 0$. The results refer to a flat MDM model with $\Omega_v = 0.3$, $\Omega_B = 0.05$, and $h = 0.5$.

of radius R. We plot $\sigma(R)$ for the following four models: SCDM, a blue (with $n = 1.2$) CDM model (BCDM), MDM, and BMDM ($n = 1.2$) with $\Omega_v = 0.3$. All models are normalized to the rms value ($\Sigma_{COBE} = 30\ \mu$K) of the temperature fluctuations in the DMR maps. Our calculation of Σ_{COBE} does not take into account the monopole and dipole subtraction from the galaxy-cut data. This underestimates the large-scale power by $\sim 15\%$ (Wright et al. 1994); note that the 1 σ experimental uncertainty is $\sim 10\%$. The reduction of power on small scales and the flattening of $\sigma(R)$ for the MDM model compared to SCDM are apparent. Our BMDM model is intermediate between SCDM and MDM. So this model can in principle be consistent with the small-scale clustering of galaxies. This alleviates the problem of the standard MDM model, where structure formation is expected to occur later than in SCDM. To roughly quantify this issue, we evaluate the redshift of formation of structures by asking when, on a given scale, a 1 σ fluctuation goes nonlinear (i.e., $\delta = 1$ in linear theory). In Table 1 we show the redshifts of nonlinearity for three mass scales ($M = 10^{12}$, 10^{13}, and $10^{14}\ M_\odot$), corresponding to typical masses of galaxies ($z_{nl,gal}$), groups ($z_{nl,gr}$), and clusters of galaxies ($z_{nl,cl}$), respectively. A more detailed discussion on the epoch of structure formation in BMDM models and a comparison with recent data on the high-redshift abun-
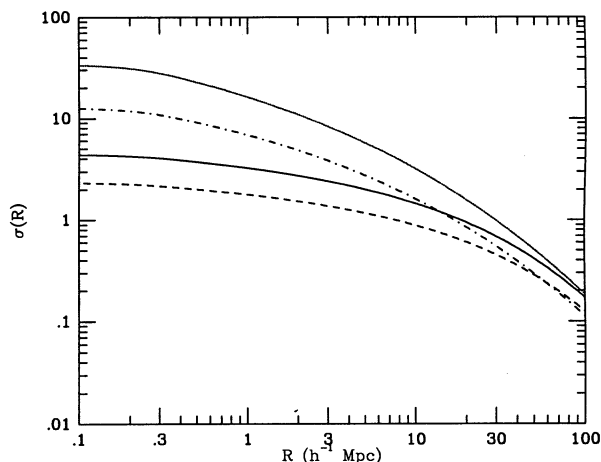
FIG. 2.—The rms value of the fluctuation density field at the present epoch, $\sigma(R)$, is plotted against the filtering scale R, in units of Mpc ($h = 0.5$ has been used). The four curves refer to the different scenarios of galaxy formation that we consider in this paper: BCDM (*dotted curve*), SCDM (*dot-dashed curve*), BMDM (*continuous curve*), and MDM (*dashed curve*). All these models have initial spectra normalized to the rms temperature fluctuation of the *COBE* DMR maps.

TABLE 1
REDSHIFT OF GALAXY, GROUP, AND CLUSTER FORMATION

Model	$z_{\mathrm{nl,gal}}$	$z_{\mathrm{nl,gr}}$	$z_{\mathrm{nl,cl}}$
SCDM.......	4.4	2.5	1.0
BCDM	11.4	6.5	3.1
MDM	0.6	0.3	0.1
BMDM......	1.9	1.3	0.7

dance of damped Lyα systems (Storrie-Lombardi et al. 1995) can be found in Borgani et al. (1995).

3.1. *Bulk Velocities*

We test our models against peculiar velocity data. We consider the Local Group (LG) velocity relative to the CMB (Kogut et al. 1993), assigning a velocity of $|v^{(1)}| = 627 \pm 22$ km s^{-1} to a sphere of radius $R_1 = 5\ h^{-1}$ Mpc. We also use recent data by Dekel (1994), which give the bulk flow $\{v^{(m)}\}$ ($m = 2, 7$) of spheres of radius $R_m = 10, 20, \ldots, 60$ h^{-1} Mpc. These data were derived after reconstructing with the POTENT method (Bertschinger et al. 1990) the three-dimensional velocity field smoothed by a Gaussian window with a radius of $R_{\mathrm{POT}} = 12\ h^{-1}$ Mpc. Therefore, in the following we will consider the set $\{v^{(m)}\}$ ($m = 1, 7$) corresponding to the LG velocity and six bulk flows.

The likelihood of the data $p(\{v^{(m)}\} \mid \mathscr{H})$ under the hypoth-

esis $\mathscr{H}$, in our case a model with a given Ω_ν and n, can be written as

$$p(\{v^{(m)}\} \mid \mathscr{H}) = \frac{1}{(2\pi)^{3N/2}} \frac{1}{|V|^{3/2}}$$
$$\times \exp\left[-\frac{1}{2} \sum_{i=1}^{N} \sum_{j=1}^{N} V_{ij}^{-1}(v^{(i)} \cdot v^{(j)}) \right], \quad (7)$$

where V_{ij}^{-1} and $|V|$ are the inverse and the determinant of the 7×7 correlation matrix, $V_{ij} \equiv \langle v^{(i)} \cdot v^{(j)} \rangle / 3$, respectively. The condition $\mathscr{H}$ is contained in the elements of the correlation matrix, which can be written as

$$V_{ij} = \frac{H_0^2}{6\pi^2} \int dk\, P(k)\tilde{W}_i(kR_i)\tilde{W}_j(kR_j)$$
$$\times \exp\left(-k^2 R_{\mathrm{POT}}^2\right) + \frac{\Sigma_{\mathrm{obs}}^{(i)2}}{3}\delta_{ij}, \quad (8)$$

where the indices i and j refer to the velocities of spheres of different radii as indicated in Table 2, $P(k)$ is the density fluctuation power spectrum of the chosen theoretical model (properly normalized to *COBE* DMR data) and $\Sigma_{\mathrm{obs}}^{(i)}$ are the observational error bars. Moreover, in equation (8), $\tilde{W}_i(kR_i) = 3j_1(kR_i)/(kR_i)^3$.

The observational data $|v_{\mathrm{obs}}^{(i)}|$ with their error bars $\Sigma_{\mathrm{obs}}^{(i)}$ are compared in Table 2 with the theoretical predictions for the three-dimensional rms bulk flows $\Sigma_v^{(i)} = (\langle|v_{\mathrm{th}}^{(i)}|^2\rangle)^{1/2} = (3V_{ii})^{1/2}$ ($i = 1, 7$), obtained for SCDM, BCDM (with $n = 1.2$), MDM, and BMDM ($n = 1.2$) with $\Omega_\nu = 0.3$. The corresponding values of the bias parameter $b \equiv \sigma^{-1}(8\ h^{-1}$ Mpc) are also given in Table 2. Note that $|v_{\mathrm{th}}^{(i)}|$ has a χ^2 distribution with 3 degrees of freedom: at the 90% confidence level $\Sigma_v/3 < |v_{\mathrm{th}}^{(i)}| < 1.6\Sigma_v/3$. Moreover, a more direct comparison between theory and observations should also take into account the directions of the single $v_{\mathrm{obs}}^{(i)}$, which are in fact considered in our likelihood analysis (cf. eq. [7]).

Now we consider models with $1 \leq n \leq 1.5$ and $\Omega_\nu \leq 0.5$, and we look for the model most consistent with the data, i.e., the one that maximizes the likelihood of the set $\{v^{(m)}\}_{\mathrm{obs}}$. We find that this happens for $\Omega_\nu = 0$ and $n = 1.1$, if we maximize the joint probability of having the measured bulk flows *and* the CMB dipole. We find instead $\Omega_\nu = 0$ and $n = 1.2$ if we maximize the conditional probability of having the measured bulk flows, under the condition that the CMB dipole has its measured value. The conditional probability is obtained by dividing equation (7) by

$$p(v^{(1)} \mid \mathscr{H}) = \frac{1}{(2\pi)^{3/2}} \frac{1}{V_{11}^{3/2}} \exp\left(-\frac{1}{2}\frac{|v^{(1)}|^2}{V_{11}}\right). \quad (9)$$

TABLE 2
BULK VELOCITIES: OBSERVATIONAL DATA AND THEORETICAL PREDICTIONS

i	R_i	$|v_{\mathrm{obs}}^{(i)}|$	$\Sigma_{\mathrm{obs}}^{(i)}$	SCDM (Bias 0.95) $\Sigma_v^{(i)}$	BCM (Bias 0.50) $\Sigma_v^{(i)}$	MDM (Bias 1.47) $\Sigma_v^{(i)}$	BMDM (Bias 0.91) $\Sigma_v^{(i)}$
1......	5	627	22	880	1387	723	1107
2......	10	494	170	509	705	488	670
3......	20	475	160	467	638	452	614
4......	30	413	150	418	562	409	548
5......	40	369	150	377	496	371	488
6......	50	325	140	338	438	335	434
7......	60	300	140	310	394	308	391

Thus, BCDM models seem to be favored from this kind of analysis.

In order to define a 95% confidence level for Ω_ν and n, we proceed as follows. We define a likelihood ratio $\lambda \equiv p(\{v^{(m)}\} \mid \mathcal{H}_1)/p(\{v^{(m)}\} \mid \mathcal{H}_2)$, and we test the condition $\mathcal{H}_1$ (a model with given Ω_ν and n) against the condition $\mathcal{H}_2$ (the most probable model). Here p is either the joint probability (of eq. [7]) or the conditional probability of reproducing the observed set $\{v^{(m)}\}_{\text{obs}}$. We generate 10,000 realizations of the set $\{v^{(m)}\}$ under $\mathcal{H}_1$ and $\mathcal{H}_2$, respectively, and from them we evaluate $p(\lambda \mid \mathcal{H}_1)$ and $p(\lambda \mid \mathcal{H}_2)$ (see Del Grande & Vittorio 1992 for more details on this method). We find that BMDM models with a small fraction of hot dark matter, $\Omega_\nu \lesssim 0.3$, can provide a reasonable agreement with the peculiar velocity data. We will compare this conclusion with the analysis of detailed N-body simulations in § 4.2.

3.2. *Cluster Abundance: The X-Ray Constraints*

In this section we test the predictions of models with primordial blue perturbation spectra against the local X-ray luminosity function (XRLF) of galaxy clusters (Kowalski et al. 1984). In hierarchical scenarios the XRLF can be derived from the cluster mass distribution using the appropriate M/L relation between the cluster mass M and its X-ray luminosity L. Considerable evidence (see, e.g., Colafrancesco & Vittorio 1994 for a discussion) suggests that the cluster mass distribution can be reasonably represented by the Press-Schechter (1974) formula

$$N(M, t) = \frac{\mathscr{I}}{M} \left| \frac{dv_c}{dM} \right| \frac{\rho}{(2\pi)^{1/2}} \exp\left(\frac{-v_c^2}{2} \right), \quad (10)$$

where $v_c \equiv \delta_c/\sigma(M, z)$, $\delta_c = 1.7$, and ρ is the mean density at time t (the mass M is defined through the corresponding radius of a top-hat filter of radius R). The normalization is uncertain within a factor $1 \lesssim \mathscr{I} \lesssim 2$ (see, e.g., Bond et al. 1991). A direct comparison of the mass distribution in equation (10) with the data of Bahcall & Cen (1992) is not straightforward, since the mass M in the Press-Schechter theory can be related to the estimated mass within a fixed radius, $M_A = M(r < 1.5 \ h^{-1} \ \text{Mpc})$ only if detailed information about the cluster density profiles is available (see, e.g., Antonuccio-Delogu & Colafrancesco 1994 for a discussion). On the contrary, the X-ray luminosities are mostly sensitive to the inner parts of the density profiles, as the specific emissivities (mainly due to thermal bremsstrahlung from the hot intergalactic medium [IGM]) are $\epsilon_\nu \sim y^{-\alpha} \exp(-y)$, where $y = h\nu/kT$ and $\alpha \approx 0.3$–0.4 (Gioia et al. 1990). So, apart from the theoretical difficulties in explaining the existence of a cluster core, the X-ray luminosity $L_x \propto \int dr \, r^2 \bar{n}^2(r) T^{1/2}(r)$ is a more reliable quantity than M_A, because of its relation to the total cluster mass M. Here $\bar{n}$ is the density of the IGM at temperature T, and the integral is extended over the cluster volume. We adopt here the following parameterization for the local cluster X-ray luminosity:

$$L \propto M^c \rho^d \mathscr{K}(\Delta E, z), \quad (11)$$

where $c = 4/3$, $d = 7/6$, and

$$\mathscr{K}(\Delta E, z) = \int_y^{y + \Delta y} dy \, \epsilon_\nu(y) \Big/ \int_0^\infty dy \, \epsilon_\nu(y)$$

is the K-correction in the energy band Δy. This correction, applied to the *HEAO 1* energy band, 2–6 keV, yields, at $z \approx 0$, a reduction of the total luminosities by a factor ~ 3 (see Colafrancesco & Vittorio 1994 for a more complete discussion).

Given $N(M, z)$ and the ratio $M/L \propto M^{1-c}$ from equation (11), we obtain the comoving XRLF

$$N(L, z) \equiv N(M, z) \frac{dM}{dL} = \frac{1}{c} \frac{M}{L} N(M(L, z, \Delta E), z). \quad (12)$$

We plot in Figure 3 the local XRLF predicted by our models, normalized as in the previous section, choosing the canonical value $\delta_c \approx 1.7$, to select collapsed objects. The XRLFs predicted in all our models are well above the observational data, indicating that *COBE* normalized models are unable to reproduce the cluster abundance, quite independently of the value of the spectral index n. If we allow for δ_c values larger than 1.7, we can reproduce the observed XRLF at a better level (see Colafrancesco & Vittorio 1994). In fact, the mass distribution in equation (12) depends upon the combination $\delta_c b$ and $\mathscr{I}$. So, for a given model (i.e., for a given Ω_ν and n), we may derive $\delta_c b$ and $\mathscr{I}$ by a direct fit to the XRLF data. The results of a χ^2 analysis are shown in Table 3. The theoretical XRLFs, obtained with the values of Table 3 for $\delta_c b$ and $\mathscr{I}$, are also shown in
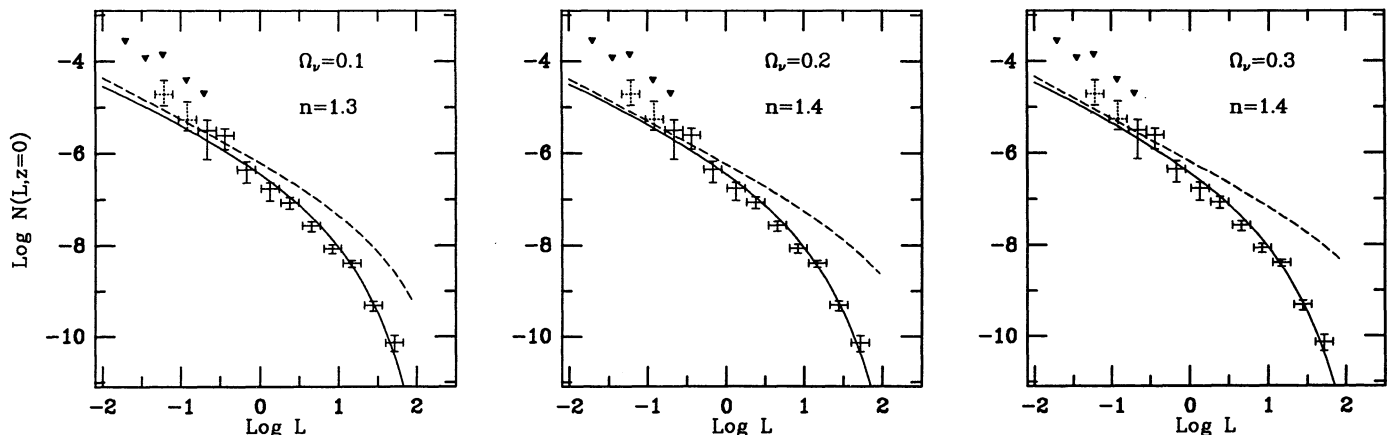

FIG. 3.—Predictions for the local X-ray luminosity function are compared with data from Kowalski et al. (1984). The dotted curves in the three panels are evaluated with the choice of parameters listed in Table 3 which gives the best fit to the data (see text for details). The dashed curves in each panel are the XRLFs obtained with $\delta_c = 1.7$ and fluctuation spectra normalized to the *COBE* DMR amplitude. X-ray luminosities are evaluated in the 2–6 keV energy band.

TABLE 3
PARAMETERS OF THE XRLF FIT

(Ω_v, n)	$\delta_c b$	$\mathscr{I}$	χ^2_{min}
(0.1, 1.3)......	2.7	1.3	1.93
(0.2, 1.4)......	2.7	1.3	1.74
(0.3, 1.4)......	2.8	1.7	1.59

Figure 3. Note that for $\Omega_v = 0.3$ and $n = 1$ the difference between the two approaches is quite small.

A discussion of the cluster abundance obtained in N-body simulations will be presented in § 4.3.

4. N-BODY SIMULATIONS

To study the large-scale structure of the universe in models with blue primordial perturbation spectra, we ran N-body simulations of the matter distribution. We used a particle-mesh code with a box of side 260 h^{-1} Mpc (we adopt here $h = 0.5$). We considered three different models: SCDM; BCDM with primordial spectral index $n = 1.2$; and BMDM, still with primordial spectral index $n = 1.2$ but with $\Omega_{CDM} = 0.65$, $\Omega_B = 0.05$, and $\Omega_v = 0.3$. We choose this last model, even if only marginally consistent with the linear analysis of the velocity field presented in § 3.1, in order to study an extreme case where the effects of the hot component can be largely appreciated; moreover, this choice allows a direct comparison with the results of Klypin et al. (1993), who simulated a model with the same Ω_v but with a primordial spectral index $n = 1$.

We define the present time by fixing the normalization to the value implied by *COBE* DMR data in the absence of any relevant gravitational wave contribution: this corresponds to approximately $b = 1$, $b = 0.5$, and $b = 0.9$, for SCDM, BCDM, and BMDM, respectively.

In the case of CDM models (SCDM and BCDM), we used 128^3 grid points and 128^3 particles. Initial conditions were set using the standard approach based on applying the Zeldovich approximation and assuming Gaussian primordial fluctuations with power spectrum $P(k) \propto k^n T^2(k)$, where $T(k) = (1 + 6.8k + 72.0k^{3/2} + 16.0k^2)^{-1}$ is the CDM transfer function (Davis et al. 1985). More details about these simulations can be found in Moscardini et al. (1995).

The presence of the neutrino component in BMDM was taken into account in the initial conditions as follows. We used the transfer functions computed in § 3 for each component separately. At redshift z the neutrinos have a thermal motion with velocity distribution given by the Fermi-Dirac statistics,

$$dn(v) \propto \frac{v^2\, dv}{\exp\,[v/v_0(z)] + 1}, \qquad (13)$$

where $v_0(z) = 7.2(1 + z)(m_v/7 \text{ eV})^{-1}$ km s^{-1}, m_v being the neutrino mass; the corresponding rms velocity is $v_{rms}(z) = 3.596 v_0(z)$. We start our simulations at $z = 20$.

Very rapidly the growth of baryonic fluctuations becomes similar to that of the cold component: because of this (see also Klypin et al. 1993), we preferred to include the baryons with the cold particles and considered only two components. Our N-body simulation of BMDM includes three sets each having 128^3 particles, one for the cold particles and two for the hot ones; the relative masses of cold and hot particles are 0.7 and 0.15, respectively. The initial conditions were generated by following the same method

used by Klypin et al. (1993), still based on the Zeldovich approximation. The displacement of the cold particles was obtained with a power spectrum where only the transfer function of the cold plus baryonic components was considered. The same random phases were used to generate the displacement of the hot particles: in this case the power spectrum contains only the transfer function for the hot component. A thermal velocity with random direction and amplitude drawn from the Fermi-Dirac distribution was added to the velocity of the hot particles. Imposing the condition that the two sets of hot particles have velocities with opposite directions avoids the generation of spurious fluctuations.

4.1. Matter Distribution

In Figure 4 we plot the projected particle positions from a slice of depth 20 h^{-1} Mpc, for the three models at the present time. A 1/4 random sampling is adopted, and only the cold particles are shown in the case of BMDM. At first glance, the resulting distributions for SCDM and BMDM are quite similar, even if in the latter case larger underdense regions are present. Structures are instead more evident for BCDM, where voids are larger, the mass distribution being more lumpy with many isolated clusters.

An interesting insight into the clustering of the mass can be obtained from the counts-in-cells analysis. In particular, we calculate the variance $\sigma^2 \equiv \langle \delta^2 \rangle$. Figure 5 shows σ^2 as a function of the side R of cubic cells for the three models at the present time; shot-noise corrections were applied. For comparison, we also show the results (with 95% error bars) obtained by Loveday et al. (1992) in the analysis of the Stromlo-APM galaxy redshift survey. According to Loveday et al. (1992), galaxies in this catalog are nearly unbiased with respect to the mass; this implies that their counts can be directly related to the matter distribution. The results we show refer to real space: we checked that redshift distortions in our simulations slightly affect the variance only on very small scales.

The SCDM model, as is already known (Efstathiou et al. 1990; Loveday et al. 1992), has too small a variance on scales ranging from 20 to 60 h^{-1} Mpc. The clustering for BCDM is too strong on small scales: σ^2 is outside the 95% observational range for $R \lesssim 35$ h^{-1} Mpc. On the contrary, the results for BMDM are very close to the observational ones.

One of the most important features of the large-scale matter distribution is the presence of large voids: for example, de Lapparent, Geller, & Huchra (1986) found in slices of the CfA survey empty regions of radius around 50 h^{-1} Mpc. More recently, Vogeley et al. (1994a) compared void statistics of the extended CfA survey with simulations of different cosmological models, finding that models with Gaussian initial fluctuations and CDM-like primordial power spectra are favored. Comparing the Perseus-Pisces survey with N-body simulations, Ghigna et al. (1994) find that a MDM model with $\Omega_{CDM}/\Omega_v/\Omega_B = 0.6/0.3/0.1$ and primordial spectral index $n = 1$ exceeds the observational void probability function for radii smaller than 10 h^{-1} Mpc, while a CDM model fares better. Statistics aiming at measuring the presence of voids in the universe are plagued by the very ambiguity in the definition of "void." For our analysis we preferred to calculate the underdensity probability function (UPF) $P_{80}(R)$, defined as the probability of having a cubic region of side R with a density more than
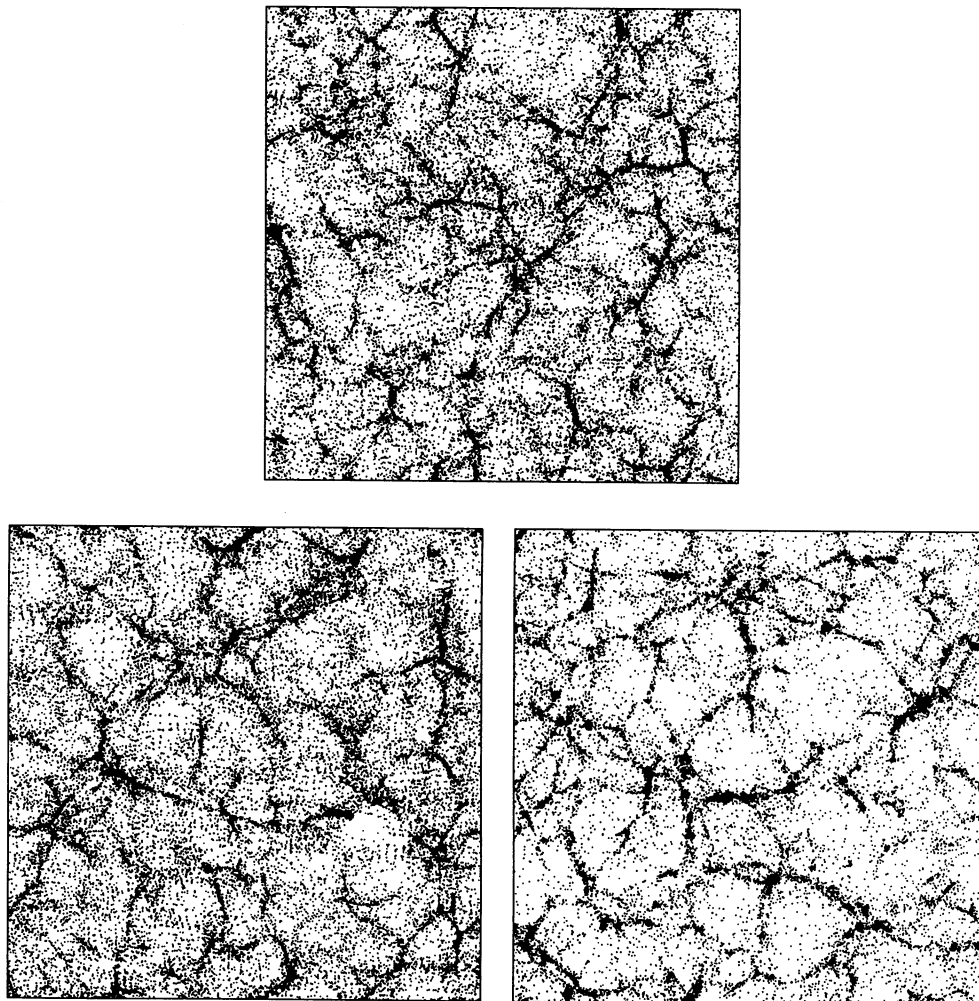
FIG. 4.—Matter distribution in slices of 20 h^{-1} Mpc for SCDM (*top*), BMDM (*lower left*), and BCDM (*lower right*), at the present time. The box refers to the whole simulation, 260 h^{-1} Mpc. A random sampling of 1/4 is adopted. For BMDM only the "cold" particles are shown.
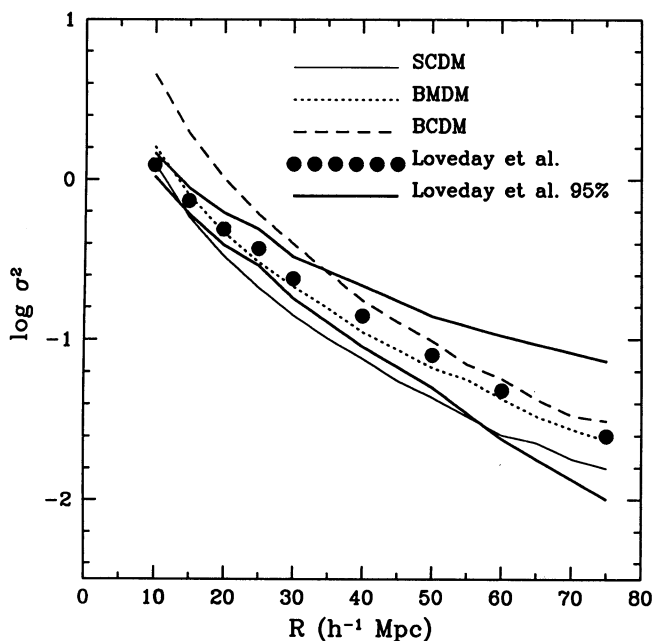

FIG. 5.—Counts-in-cells analysis: the variance σ^2 as a function of the side R of cubic cells for SCDM (*solid line*), BMDM (*dotted line*), and BCDM (*dashed line*). Filled circles and heavy solid lines refer to the Loveday et al. (1992) analysis of the Stromlo–APM catalog and their 95% confidence level, respectively.

80% below the mean (i.e., $\delta < -0.8$). This statistic is less sensitive to the estimate of the mean density and to shot noise, and permits us to probe larger scales (being nonzero for larger R) than the usual void probability function. Figure 6 shows P_{80} as a function of R. As expected, and in agreement with the analysis of Piran et al. (1993), a blue primordial spectrum increases the presence of large voids. In fact, while the probability for SCDM goes to zero for $R \approx 25\ h^{-1}$ Mpc, BMDM and BCDM have nonzero P_{80} out to 30 and 40 h^{-1} Mpc, respectively. For small-scale voids, SCDM and BMDM behave in a very similar way; on the contrary as is also evident from the slice in Figure 4, BCDM also presents a large amount of small voids.

Another test of the matter distribution we consider is the mean *contour genus* per unit volume, g_S. Recently, Vogeley et al. (1994b), performing a topological analysis of the CfA redshift survey, found that SCDM has too large an amplitude on smoothing scales $\lesssim 10\ h^{-1}$ Mpc, while an open CDM model and a CDM model with nonzero cosmological constant are always consistent with the observed genus. Figure 7 shows, for the three models at the present time, the g_S curves obtained using the program by Weinberg (1988). The simulated data have been filtered by a Gaussian window, $W(r) = (\pi^{3/2}\lambda^3)^{-1} \exp(-r^2/\lambda_e^2)$, with two different radii, $\lambda_e = 6\ h^{-1}$ Mpc and $\lambda_e = 20\ h^{-1}$ Mpc, in order to
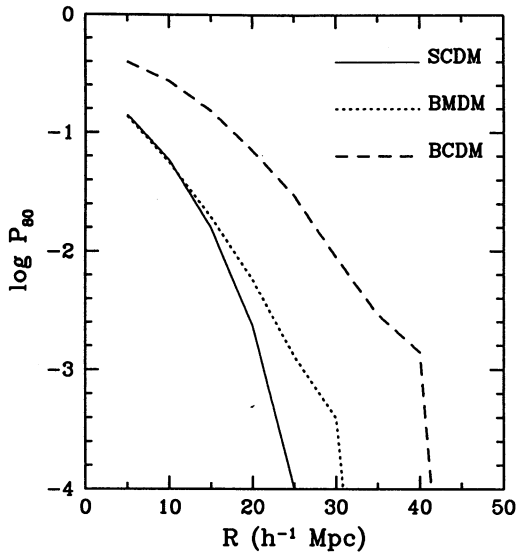
FIG. 6.—Underdensity probability function P_{80} as a function of side R of cubic cells for SCDM (*solid line*), BMDM (*dotted line*), and BCDM (*dashed line*).

examine the topology of structure on both nonlinear and linear scales. For ease of comparison with Vogeley et al. (1994b), we consider contours of fixed volume fraction, and we plot g_S as a function of the threshold v parameterizing the volume fraction in a Gaussian field:

$$F_{\text{vol}} = (2\pi)^{-1/2} \int_v^\infty \exp{(-t^2/2)}dt \; .$$

Moreover, we normalize the genus curves using the volume of the CfA1+2 survey. Error bars, obtained by a bootstrap technique, are always smaller than 10%; in the interest of clarity they are not shown in the figure. For a Gaussian random field (e.g., Doroshkevich 1970),

$$g_S = g_0(1 - v^2) \exp{(-v^2/2)} \; , \qquad (14)$$

where the normalization g_0 is related to the power spectrum of density fluctuations $P(k)$ through

$$g_0 = \frac{1}{4\pi^2} \left[\frac{\int dk\, k^4 P(k)}{3 \int dk\, k^2 P(k)} \right]^{3/2} . \qquad (15)$$
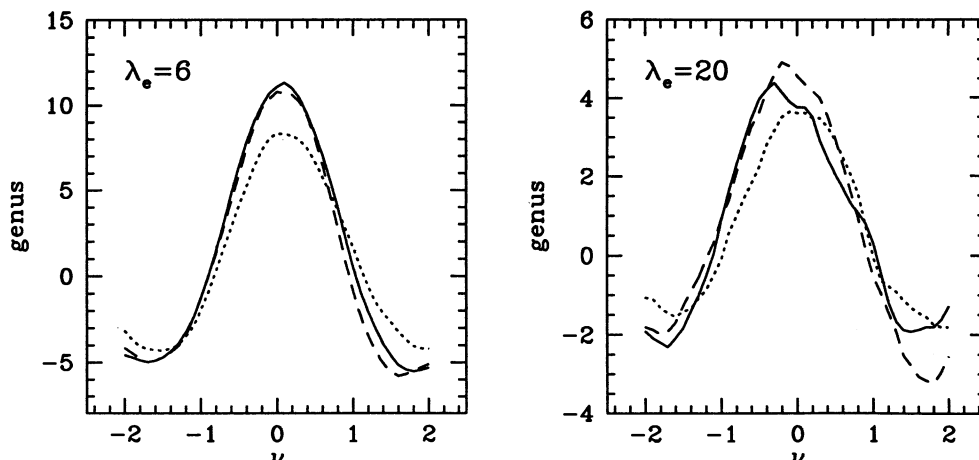
The action of gravity changes the underlying statistics for the density fluctuation δ, breaking the symmetry of g_S. A shift of the peak of the genus curve toward either high or low density reflects a topology that is bubble-like or meatball-like, respectively. In order to quantify this shift, we use a statistic Δv (e.g., Park, Gott, & da Costa 1992; Vogeley et al. 1994b) defined as

$$\Delta v = \int_{-1}^1 dv\, vg(v)_{\text{obs}} \Big/ \int_{-1}^1 dv\, g(v)_{\text{fit}} \; , \qquad (16)$$

where $g(v)_{\text{obs}}$ and $g(v)_{\text{fit}}$ are the measured and the best-fit random-phase genus curves, respectively. In agreement with the previous definition, Δv is positive (negative) when the genus curve has a bubble (meatball) shift. In Table 4 we compare the results for g_0 and Δv at the two filtering radii for our three models and the CfA1+2 sample. In agreement with Vogeley et al. (1994b), SCDM is found not to reproduce the observed topology in the nonlinear regime: the amplitude of g_0 at $\lambda_e = 6\ h^{-1}$ Mpc is too large and the bubble shift too small; moreover, at $\lambda_e = 20\ h^{-1}$ Mpc the peak shift is in the wrong direction. A similar negative trend is shown by BCDM, at both small and large smoothing. On the contrary, BMDM has the desired behavior: the CfA1+2 data are well inside the error bars.

4.2. Velocity-Field Statistics

In order to recover the velocity field from each simulation, we follow a standard procedure (e.g., Kofman et al. 1994). First, we interpolate the mass and momentum from the particle distribution onto a cubic grid with 128^3 grid points, using a triangular shaped cloud algorithm (see, e.g., Hockney & Eastwood 1981); we then further smooth by a Gaussian filter with width $2\ h^{-1}$ Mpc, to ensure a nonzero density at every grid point. The velocity at each grid point is defined as the momentum divided by the mass density. Because the velocity field is quite sensitive to long-wavelength fluctuations, following Strauss, Cen, & Ostriker (1993) and Lucchin et al. (1995), we included in our simulations the effect of waves larger than the box size. To do so, we added to the velocity of each particle the linear rms bulk velocity of a cube of $260\ h^{-1}$ Mpc, the size of our simulations. The direction of the bulk velocity was chosen at random for each simulation. The value of such a bulk flow

FIG. 7.—Mean contour genus as a function of the effective threshold v for SCDM (*solid line*), BMDM (*dotted line*), and BCDM (*dashed line*). Two different Gaussian filtering radii are considered: $\lambda_e = 6\ h^{-1}$ Mpc (*left*) and $\lambda_e = 20\ h^{-1}$ Mpc (*right*).

TABLE 4

Topological Statistics

	$\lambda_e = 6\ h^{-1}$ Mpc		$\lambda_e = 20\ h^{-1}$ Mpc	
	g_0	Δv	g_0	Δv
CfA1+2......	7.70	0.19	4.00	0.14
SCDM	11.37 ± 2.09	0.07 ± 0.12	3.98 ± 1.30	-0.13 ± 0.14
BCDM	11.11 ± 1.97	0.05 ± 0.13	5.02 ± 1.28	-0.07 ± 0.14
BMDM	8.47 ± 1.75	0.13 ± 0.12	3.77 ± 1.09	0.05 ± 0.16

is approximately 220 km s^{-1} for SCDM and 250 km s^{-1} for both BMDM and BCDM.

The left-hand panel of Figure 8 shows the velocity modulus $v \equiv |v|$ distribution function $P(v)$ for our models. The blue models generally produce larger flows. The difference is statistically significant: in BCDM and BMDM there are respectively about 700 and 13,000 grid points with a velocity greater than 2000 km s^{-1}, whereas SCDM contains no grid point with such a high velocity.

To further characterize the velocity field of each model, we computed the bulk flow, i.e., the amplitude of the center-of-mass velocity of a sphere: $v_{\rm bulk}(R) = |\sum_{i=1}^{n} v_i|/n$, where the sum extends over the n grid points falling within a distance R from the center. In order to compare our results with observational data from the POTENT analysis (e.g., Dekel 1994) we smooth the simulated velocity field by a Gaussian filter of radius 12 h^{-1} Mpc. In particular, the bulk flow is calculated for each model by randomly selecting 100 different grid points from the simulations and calculating the statistics in top-hat spheres, of radius ranging from 10 to 130 h^{-1} Mpc, centered on them. The central panel of Figure 8 shows the values obtained by averaging the results over the 100 estimates. Error bars, which are in all cases less than 5%, have not been plotted for clearness. Due to the large error bars in POTENT data, all three models are in good agreement with observations. As expected, the larger flows in blue models displayed by the $P(v)$ analysis imply higher bulk flows. Of course, having larger data samples, such as the "Mark III" compilation (Willick et al. 1995), can help to increase the discriminatory power of this statistical test on the large-scale velocity field.

Another relevant statistic for the peculiar velocity field is the cosmic Mach number, $\mathcal{M}$ (Ostriker & Suto 1990), defined as the ratio of the bulk flow to the one-point velocity dispersion σ_v: $\mathcal{M}(R) = v_{\rm bulk}(R)/\sigma_v(R)$, where $\sigma_v^2(R) = \sum_{i=1}^{n} (v_i - v_{\rm bulk})^2/n$ and the sum is extended over the same grid points. Since the bulk flow is caused by density fluctuations on scales larger than the sampled volume, while the velocity dispersion mostly depends on the power on smaller scales, $\mathcal{M}$ actually measures the ratio of large- to small-scale power in the velocity field. The mean values of $\mathcal{M}$, obtained in the same way as for the bulk flows, are also shown in Figure 8 (*right-hand panel*), for the three models at the present time (where error bars, always less than 10%, are not plotted). The estimates for SCDM and BMDM are very close and always inside the error bars. On the contrary, the cosmic Mach number for BCDM is larger; this is due to the higher values of $v_{\rm bulk}$ obtained for this model on small scales.

4.3. *Cluster Analysis*

In order to identify clusters in our simulations, we adopted a standard method (White et al. 1987; Jing et al. 1994; Jing & Fang 1994; Croft & Efsthathiou 1994). As a first step, we adopt a friends-of-friends algorithm to extract the groups of cold particles with a linking parameter equal to one-fifth of the mean separation of the cold particles. After finding the center of mass of the groups, we calculate the total (i.e., cold plus hot) mass inside a sphere of radius $r_{\rm cl} = 1.5\ h^{-1}$ Mpc, roughly corresponding to the radius of Abell clusters. When the distance between the centers of two cluster candidates is smaller than $2r_{\rm cl}$, we eliminate from the
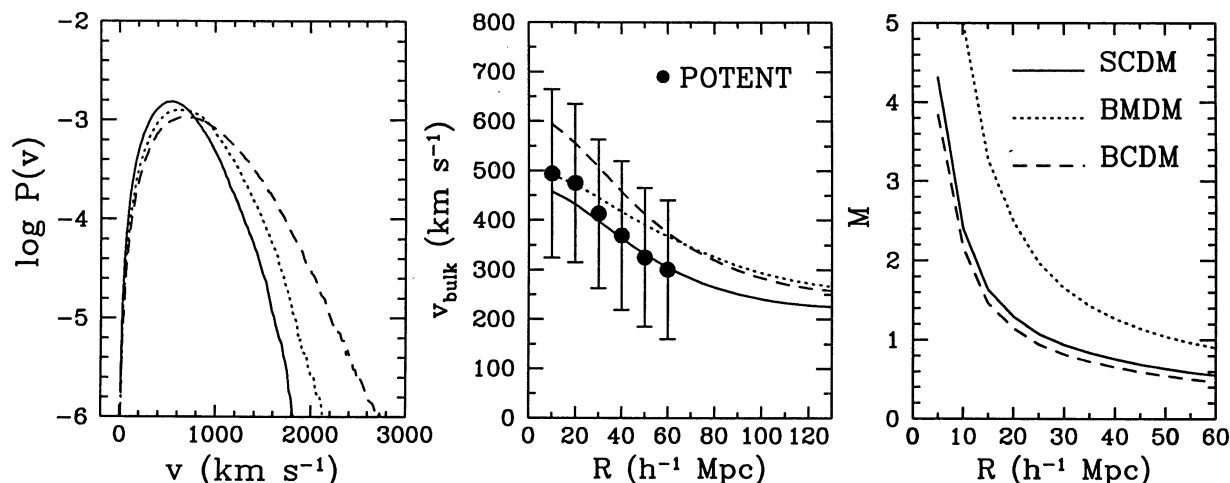

Fig. 8.—Velocity-field statistics. Different lines refer to different models: SCDM (*solid line*), BMDM (*dotted line*), and BCDM (*dashed line*). *Left*: Distribution function of the velocity modulus v. *Center*: Bulk flow as a function of the radius R of the sphere. Filled circles and error bars refer to the POTENT data (Dekel 1994). *Right*: Cosmic Mach number as a function of the radius R of the sphere.
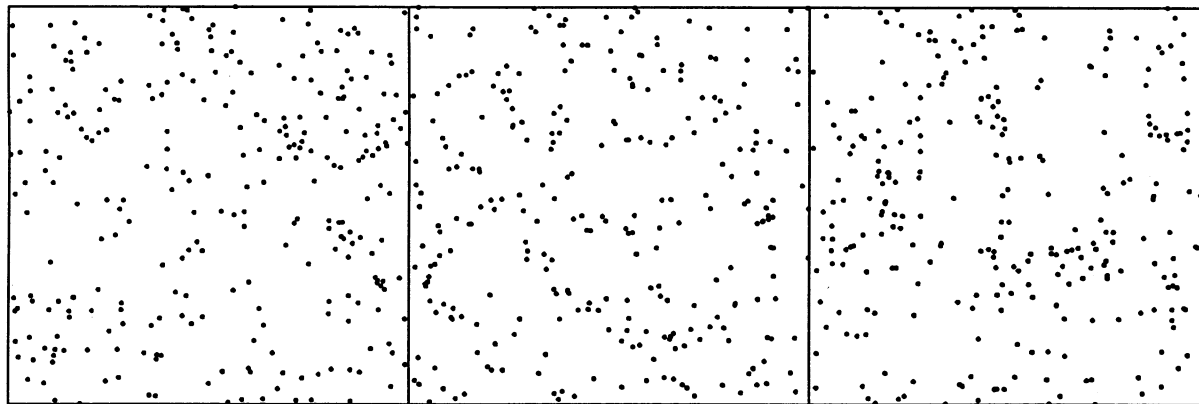
FIG. 9.—Projected distribution of clusters identified with an intercluster distance of $40\ h^{-1}$ Mpc. The box represents the whole simulation ($260\ h^{-1}$ Mpc side): SCDM (*left*), BMDM (*center*), and BCDM (*right*).

list the cluster with the smaller mass, and we repeat the whole procedure using all particles not belonging to "clusters," until the number of clusters does not change: in this way we can take into account the possible presence of more clusters in overdense regions and/or filaments (i.e., superclusters) which would be merged by the percolation algorithm.

In Figure 9 we show the spatial distribution of clusters obtained in our simulations. In this plot, we consider only the richest clusters, i.e., those with a mass larger than a suitable threshold chosen to reproduce the mean density of the ACO/Abell catalog, corresponding to an intercluster separation $d_c \approx 40\ h^{-1}$ Mpc.

The cumulative mass function $n(>M)$, i.e., the number of clusters per unit volume with a mass larger than M, is presented for the three models in Figure 10. The BCDM model has a larger number of rich clusters compared with SCDM and BMDM, which behave in a similar way. A comparison with the observational estimates can be done using the mass function derived by Bahcall & Cen (1992) using both optical (richness, velocities, and the luminosity function of galaxies in clusters) and X-ray data (temperature distribution of clusters). All models present too high a mass function for larger masses. The disagreement already known in the case of SCDM (e.g., Bahcall & Cen 1992; Jing & Fang 1994), is significant: for example, no object with mass larger than $10^{15}\ M_\odot$ is found in the Bahcall & Cen (1992) data, while these objects may be found in the simulations. However, according to Klypin & Rhee (1994), the estimates of Bahcall & Cen (1992) should be reconsidered, because of some underlying assumptions, such as the density profile or sphericity. Independent estimates of the cluster mass function, using masses derived directly from the dynamics (i.e., virial evaluations), give higher values for the mass function (Biviano et al. 1993). Data from Bahcall & Cen (1992) and Biviano et al. (1993) are also shown in Figure 10; in the latter case error bars account for uncertainties both in the best-fit parameters and in the cluster mean density. Considering the Biviano et al. (1993) data, the agreement with BMDM and SCDM is definitely better, while the number of very rich clusters is still a problem for the BCDM model.

These results are in good agreement with the linear cluster analysis discussed in § 3.2. All the considered models tend to overestimate the cluster abundance, as is clear from the fact that the Press-Schechter formula fits the Bahcall & Cen (1992) data only provided that the threshold is chosen

to take high values, such as $\delta_c \sim 2.5$, which is equivalent to an artificially low normalization (high b) for these models. If, on the other hand, the cluster abundance had been used as a constraint to fix the power-spectrum normalization (as done, e.g., by Pogosyan & Starobinsky 1995), a value of σ_8 in contrast to the amplitude required by *COBE* data would have resulted.

For our simulated cluster catalogs we compute also the two-point correlation function ξ_{acc}. Observational estimates of ξ_{cc} are well fitted by the relation $\xi_{cc} = (r/r_0)^{-1.8}$. The amplitude of the correlation function and its possible dependence on the cluster richness are rather controversial: recent estimates of r_0 based on different samples range from 13 to 25 h^{-1} Mpc (e.g., Nichol, Briel, & Henry 1994 and references therein). Figure 11 shows the results for the cluster catalogs in our simulations. For clearness, error bars, obtained by bootstrap resampling, are only shown for BMDM. As already known (see, e.g., Bahcall & Cen 1992), the cluster correlation function for SCDM is too low. On the other hand, BCDM cannot reproduce the right slope: in fact, this model is overclustered at small scales and under-
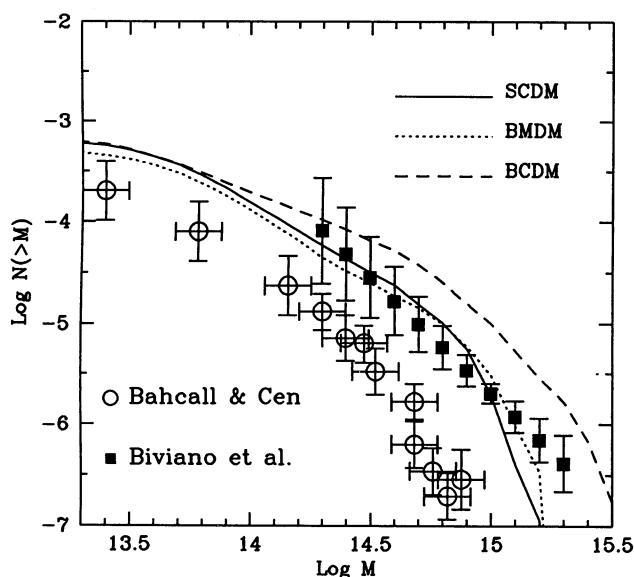

FIG. 10.—Cluster mass function $N(>M)$ (M in units of the solar mass) for SCDM (*solid line*), BMDM (*dotted line*), and BCDM (*dashed line*). For comparison the observational estimates by Bahcall & Cen (1992) and Biviano et al. (1993) are shown by open circles and filled squares, respectively.
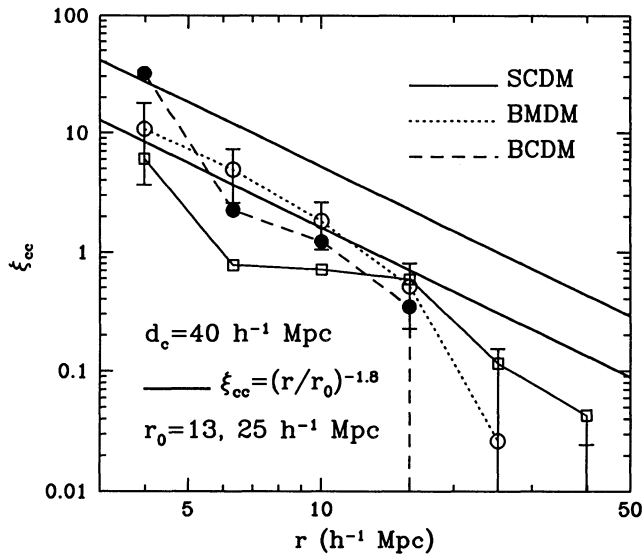
Fig. 11.—Cluster correlation function ξ_{cc} as a function of the distance r for SCDM (*solid line and open squares*), BMDM (*dotted line and open circles*), and BCDM (*dashed line and filled circles*). Bootstrap errors are shown only for BMDM. For comparison, the two heavy solid lines represent the power law $\xi_{cc} = (r/r_0)^{-1.8}$, with $r_0 = 13$ and $25\ h^{-1}$ Mpc.

clustered at larger scales. Only the results for BMDM are well inside the observational range: in this case r_0 is approximately $16\ h^{-1}$ Mpc, consistent with the standard relation $r_0 \simeq 0.4 d_c$ (Bahcall & Burgett 1986; Bahcall & Cen 1992; see also Borgani, Coles, & Moscardini 1994; Walter & Klypin 1995).

5. CONCLUSIONS

In this work we presented a detailed comparison of cold and mixed dark matter models, with blue primordial power spectra, with observational data on large scales. In our analysis we used both linear and nonlinear techniques. Let us stress that this new class of models, based on the assumption that $n > 1$, has the same level of naturalness as those based on any other choice of the primordial spectral index, such as the usual scale-invariant $n = 1$ value or the tilted, $n < 1$, ones. Being primordially scale-free, our initial conditions are more natural than those where the power spectrum contains a built-in characteristic scale. Blue types of spectra are suggested by the need of reconciling the amount of power required on large (i.e., in the range 10–100 Mpc) scales with the amplitude of perturbations implied by *COBE* data on larger scales. An unavoidable consequence of this choice, in the frame of cold dark matter models, is an excessive level of fluctuations on small (i.e., $\lesssim 1$ Mpc) scale. This is the strongest motivation for resorting to the free-streaming effect of a hot dark matter component. Indeed, the models which fare better in most of our analyses are the BMDM ones. Since our analysis assumes the *COBE* DMR data as a normalization constraint, the first test to consider is the level of temperature fluctuations on degree scale. De Bernardis et al. (1995) tested BMDM models with a late, sudden reionization of the intergalactic medium against the ARGO (de Bernardis et al. 1994), *COBE* DMR (Bennett et al. 1994), MAX (Devlin et al. 1994), and MSAM (Cheng et

al. 1994) data set. Their likelihood analysis indicates that mixed dark matter models with blue power spectra ($n \sim 1.2$) and a reionization at $z \sim 30$ are most consistent with the data, even if the standard model with $n = 1$ and without late reionization is statistically indistinguishable from the best model. It is not a problem to have a late reionization in the context of blue models. Indeed, they can have enough small-scale power at early times to produce an early generation of structures, leading to late reionization (e.g., Carr et al. 1994). Related to this property is also an anticipation of the galaxy and cluster formation epochs compared to the scale-invariant MDM case (see, e.g., Lyth & Liddle 1995; Borgani et al. 1995).

The large-scale matter distribution emerging from our BMDM scenario has the right properties to fit the existing observational data on various statistics, such as the counts-in-cells analysis of Stromlo-APM galaxies and the topology of the CfA redshift survey; thanks to the increased power on large scales compared to SCDM and MDM, the large-scale voids in our simulations also appear in good shape to reproduce the amount and size of those observed in galaxy catalogs. We also computed, both within linear theory and by numerical simulations, the large-scale peculiar velocity field, and performed a statistical comparison with observational data from POTENT (e.g., Dekel 1994): although the best model selected by a likelihood analysis is the blue CDM one, we find that BMDM models, with a small fraction of hot dark matter, can generally provide a reasonable agreement with the peculiar velocity data.

A problem which remains unsolved in the frame of all the models we considered is related to the cluster abundance. The general tendency is to produce too many massive clusters. This problem can be alleviated by considering mixed dark matter models with two nearly degenerate (in mass) neutrinos (e.g., Klypin, Nolthenius, & Primack 1995b; Babu, Schaefer, & Shafi 1995). Our analysis, in this respect, strongly differs from that of Pogosyan & Starobinsky (1995), who normalized their power spectra to fit the cluster abundance, as deduced by a Press-Schechter formula, with the Bahcall & Cen (1992) data. For us, instead, once the *COBE* DMR normalization has been imposed on the models, we obtain the cluster mass function as a *prediction* of our analysis. We believe, on the other hand, that many aspects of the cluster distribution represent an open problem for all *natural* (i.e., not containing ad hoc parameters) scenarios of structure formation, whose solution would probably require a better modeling of cluster formation in numerical simulations than is presently possible by collisionless codes.

REFERENCES

Antonuccio-Delogu, V., & Colafrancesco, S. 1994, ApJ, 427, 72
Babu, K. S., Schaefer, R. K., & Shafi, Q. 1995, preprint ASTRO-PH/ 9507006
Bahcall, N. A., & Burgett, W. S. 1986, ApJ, 300, L35
Bahcall, N. A., & Cen, R. 1992, ApJ, 398, L81
Bennett, C. L., et al. 1994, ApJ, 436, 423
Bertschinger, E., Dekel, A., Faber, S. M., Dressler, A., & Burstein, D. 1990, ApJ, 364, 370
Biviano, A., Girardi, M., Giuricin, G., Mardirossian, F., & Mezzetti, M. 1993, ApJ, 411, L11
Bond, J. R., Cole, S., Efstathiou, G., & Kaiser, N. 1991, ApJ, 370, 440
Bonometto, S. A., Lucchin, F., Occhionero, F., & Vittorio, N. 1984, A&A, 138, 477
Borgani, S., Coles, P., & Moscardini, L. 1994, MNRAS, 271, 223
Borgani, S., Lucchin, F., Matarrese, S. P., & Moscardini, L. 1995, MNRAS, in press
Carr, B. J., Gilbert, J. H., & Lidsey, J. 1994, Phys. Rev. D, 50, 4853
Carr, B. J., & Lidsey, J. 1993, Phys. Rev. D, 48, 543
Cen, R., & Ostriker, J. P. 1994, ApJ, 431, 451
Cheng, E. S., et al. 1994, ApJ, 422, L37
Colafrancesco, S., & Vittorio, N. 1994, ApJ, 422, 443
Copeland, E. J., Liddle, A. R., Lyth, D. H., Stewart, E. D., & Wands, D. 1994, Phys. Rev. D, 49, 6410
Croft, R. A. C., & Efstathiou, G. 1994, MNRAS, 267, 390
Davis, M., Efstathiou, G., Frenk, C. S., & White, S. D. M. 1985, ApJ, 292, 371
Davis, M., Summers, F. J., & Schlegel, M. 1992, Nature, 359, 393
de Bernardis, P., Balbi, A., & Vittorio, N. 1995, preprint
de Bernardis, P., et al. 1994, ApJ, 422, L33
de Gasperis, G., Muciaccia, P. F., & Vittorio, N. 1995, ApJ, 439, 1
Dekel, A. 1994, ARA&A, 32, 371
de Lapparent, V., Geller, M. J., & Huchra, J. P. 1986, ApJ, 302, L1
Del Grande, P., & Vittorio, N. 1992, ApJ, 397, 26
Devlin, M., et al. 1994, ApJ, 430, L1
Doroshkevich, A. G. 1970, Astrophysics, 6, 320
Efstathiou, G., Kaiser, N., Saunders, W., Lawrence, A., Rowan-Robinson, M., Ellis, R. S., & Frenk, C. S. 1990, MNRAS, 247, 10P
Geller, M. J., & Huchra, J. P. 1989, Science, 246, 897
Ghigna, S., Borgani, S., Bonometto, S. A., Guzzo, L., Klypin, A., Primack, J. R., Giovanelli, R., & Haynes, M. P. 1994, ApJ, 437, L71
Gioia, I. M., Maccacaro, T., Schild, R. E., Wolter, A., Stocke, J. T., Morris, S. L., & Henry, J. P. 1990, ApJS, 72, 567
Górski, K. M., Hinshaw, G., Banday, A. J., Bennett, C. L., Wright, E. L., Kogut, A., Smoot, G. F., & Lubin, P. 1994, ApJ, 430, L89
Gundersen, et al. 1993, ApJ, 413, L1
Hancock, S., Davies, R. D., Lasenby, A. N., Gutierrez de la Cruz, C. M., Watson, R. A., Rebolo, R., & Beckman, J. E. 1994, Nature, 367, 333
Hockney, R., & Eastwood, J. W. 1981, Computer Simulation Using Particles (New York: McGraw-Hill)
Hu, W., Scott, D., & Silk, J. 1994, ApJ, 430, L97
Jing, Y. P., & Fang, L. Z. 1994, ApJ, 432, 438
Jing, Y. P., Mo, H. J., Borner, G., & Fang, L. Z. 1994, A&A, 243, 295
Klypin, A., Borgani, S., Holtzman, J., & Primack, J. 1995a, ApJ, 444, 1
Klypin, A., Holtzman, J., Primack, J., & Regős, E. 1993, ApJ, 416, 1
Klypin, A., Nolthenius, R., & Primack, J. 1995b, ApJ, in press

Klypin, A., & Rhee, G. 1994, ApJ, 428, 399
Kofman, L., Bertschinger, E., Gelb, J. M., Nusser, A., & Dekel, A. 1994, ApJ, 420, 44
Kogut, A., et al. 1993, ApJ, 419, 1
Kowalski, M. P., Ulmer, M. P., Cruddace, R. G., & Wood, K. S. 1984, ApJS, 56, 403
Lauer, T., & Postman, M. 1994, ApJ, 425, 418
Liddle, A. R., & Lyth, D. H. 1993, MNRAS, 265, 379
Linde, A. 1991a, Phys. Lett. B, 249, 18
———. 1991b, Phys. Lett. B, 259, 38
———. 1994, Phys. Rev. D, 49, 748
Louis, W. C. 1994, paper presented at XVI Conf. on Neutrino Phys. and Astrophys., Eilat, Israel
Loveday, J., Efstathiou, G., Peterson, B. A., & Maddox, S. J. 1992, ApJ, 400, L43
Lucchin, F., & Matarrese, S. 1985, Phys. Rev. D, 32, 1316
Lucchin, F., Matarrese, S., Messina, A., Moscardini, L., & Tormen, G. 1995, MNRAS, 272, 859
Lyth, D. H., & Liddle, A. R. 1995, Ap. Lett. & Comm., in press
Ma, C. P., & Bertschinger, E. 1994, ApJ, 434, L5
Mather, J. C., et al. 1994, ApJ, 420, 439
Mo, H. J., Jing, Y. P., & Borner, G. 1993, MNRAS, 264, 825
Mollerach, S., Matarrese, S., & Lucchin, F. 1994, Phys. Rev. D, 50, 4835
Moscardini, L., Tormen, G., Matarrese, S., & Lucchin, F. 1995, ApJ, 442, 469
Nichol, R. C., Briel, U. G., & Henry, J. P. 1994, MNRAS, 265, 867
Ostriker, J. P., & Suto, Y. 1990, ApJ, 348, 378
Park, C., Gott, J. R., & da Costa, L. N. 1992, ApJ, 392, L51
Peebles, P. J. E. 1981, ApJ, 248, 885
Piran, T., Lecar, M., Goldwirth, D. S., da Costa, L. N., & Blumenthal, G. R. 1993, MNRAS, 265, 681
Plionis, M., Borgani, S., Moscardini, L., & Coles, P. 1995, ApJ, 441, L57
Pogosyan, D., & Starobinsky, A. 1995, ApJ, 447, 465
Press, W. H., & Schechter, P. L. 1974, ApJ, 187, 425
Schaefer, R. K., & Shafi, Q. 1993, Phys. Rev. D, 47, 1333
Smoot, G. F., et al. 1992, ApJ, 396, L1
Storrie-Lombardi, L. J., McMahon, R. G., Irwin, M. J., & Hazard, C. 1995, in Proc. ESO Workshop on QSO Absorption Lines (Berlin: Springer), in press
Strauss, M. A., Cen, R., & Ostriker, J. P. 1993, ApJ, 408, 389
Vogeley, M. S., Geller, M. J., Park, C., & Huchra, J. P. 1994a, AJ, 108, 745
Vogeley, M. S., Park, C., Geller, M. J., Huchra, J. P., & Gott, J. R. 1994b, ApJ, 420, 525
Walter, C., & Klypin, A. 1995, preprint ASTRO-PH/9507074
Weinberg, D. H. 1988, PASP, 100, 1373
White, S. D. M., Efstathiou, G., & Frenk, C. S. 1993, MNRAS, 262, 1023
White, S. D. M., Frenk, C. S., Davis, M., & Efstathiou, G. 1987, ApJ, 313, 505
Willick, J. A., Courteau, S., Faber, S. M., Burstein, D., & Dekel, A. 1995, ApJ, 446, 12
Wright, E. L., Smoot, G. F., Kogut, A., Hinshaw, G., Tenorio, L., Lineweaver, C., Bennett, C. L., & Lubin, P. M. 1994, ApJ, 420, 1
Zurek, W. H., Quinn, P. J., Salmon, J. K., & Warren, M. S. 1994, ApJ, 431, 559